



Research article

Peculiarities of charge compensation in lithium-doped hydroxyapatite

Margarita A. Goldberg^{a,*}, Marat R. Gafurov^b, Olga N. Makshakova^c,
Sergey V. Smirnov^a, Alexander S. Fomin^a, Fadis F. Murzakhonov^b, Vladimir
S. Komlev^{a,**}

^a A.A. Baikov Institute of Metallurgy and Materials Science, Russian Academy of Sciences, Moscow, 119334, Russian Federation

^b Kazan Federal University, Kazan, 420111, Russian Federation

^c Kazan Institute of Biochemistry and Biophysics, FRC Kazan Scientific Center of RAS, Kazan, 420111, Russian Federation

ARTICLE INFO

Keywords:

Hydroxyapatite

Lithium

EPR

Density functional theory

ABSTRACT

Hydroxyapatite (HA) remains one of the most popular materials for various biomedical applications and its fields of application have been expanding. Lithium (Li^+) is a promising candidate for modifying the biological behavior of HA. Li^+ is present in trace amounts in the human body as an alkaline and bioelectric material. At the same time, the introduction of Li^+ into the HA structure required charge balance compensation due to the difference in oxidation degree, and the scheme of this compensation is still an open question. In the present work, the results of the theoretical and experimental study of the Li^+ -doped HA synthesis are presented. According to X-ray diffraction data, Fourier transform infrared spectroscopy as well as the combination of electron paramagnetic resonance methods, the introduction of Li^+ in the amount up to 0.05 mol% resulted in the preservation of the HA structure. Density functional theory calculations show that Li^+ preferentially incorporates into the Ca (1) position with a small geometry perturbation. The less probable positioning in the Ca (2) position leads to a drastic perturbation of the anion channel.

1. Introduction

Hydroxyapatite (HA, $\text{Ca}_{10}(\text{PO}_4)_6(\text{OH})_2$) remains one of the most popular materials for various biomedical applications in the form of nanocomposites, coatings, scaffolds, cements, 3D printed implants, etc. due to its similarity to the inorganic component of native bone tissue [1–3]. The HA unit cell is characterized by four different types of crystallographic positions. Four calcium ions per unit cell, called Ca (1), are arranged in columns parallel to the c-axis and are surrounded by nine oxygen atoms. Other calcium ions, six per unit cell, called Ca (2), form two equilateral triangles along the c axis at $z = 1/4$ and $3/4$, a so-called anion channel. Hydroxyl groups are located on the hexagonal c-axis. The structure is completed by six PO_4^{3-} anions, each P atom coordinated by four oxygen atoms [4]. The introduction of different ions contributes to the significant changes in the properties of HA. The element lithium (Li^+) is a promising candidate for modifying the biological behaviour of HA. Li^+ is present in trace amounts in the human body as an alkaline and

* Corresponding author.

** Corresponding author.

E-mail addresses: mgoldberg@imet.ac.ru (M.A. Goldberg), komlev@mail.ru (V.S. Komlev).

<https://doi.org/10.1016/j.heliyon.2024.e25291>

Received 26 September 2023; Received in revised form 9 January 2024; Accepted 24 January 2024

Available online 6 February 2024

2405-8440/Â© 2024 Published by Elsevier Ltd. This is an open access article under the CC BY-NC-ND license (<http://creativecommons.org/licenses/by-nc-nd/4.0/>).

bioelectric material [5]. The release of Li^+ led to an improvement in the biological response of the implanted materials, which was reflected in the growth, proliferation, and differentiation of osteoblast cells via stimulation of the Wnt signalling pathway and resulting in enhanced bone regeneration *in vivo* [6,7]. Another point is related to the highly effective antibacterial capabilities of the Li^+ -containing HA nanocomposites and nanoparticles [8,9]. The introduction of Li^+ led to an intensification of sintering [10] and could improve the strength and toughness of HA ceramics [11]. The presence of Li^+ in the crystal lattices of HA and β -tricalcium phosphate (β -TCP) resulted in increased thermal stability of ceramic materials [12,13].

The improved sintering of the Li^+ -doped HA was related to the formation of cation vacancies due to the difference in oxidation state of Ca^{2+} and Li^+ . On the other hand, Li^+ as a monovalent ion required charge balance compensation for successful substitution of Ca^{2+} in the HA or β -TCP crystal lattice, which could be achieved, for example, by co-precipitation of HA in the presence of Li^+ and CO_3^{2-} ions [14]. At the same time, the mechanism of the charge balance of the single Li^+ -doped HA is still an open question.

The aim of this work was the synthesis of the lithium substituted HA powders with the low Li^+ content in the range of 0.01–0.05 mol.% by the precipitation with ripening in mother solution technique previously developed earlier by our scientific groups [15]. The influence of the lithium content on the phase composition, functional groups, degree of crystallinity, lattice parameters, and electron paramagnetic resonance (EPR) spectra is followed. The experimental results obtained are compared with the Density Functional Theory (DFT) calculations performed.

2. Materials and methods

2.1. Powders synthesis

Samples of LiHA with the chemical formula $\text{Ca}_{10-x/2}\text{Li}_x(\text{PO}_4)_6(\text{OH})_2$ were synthesized with $x = 0; 0.01; 0.04; 0.05$ (samples assignation: HA; LiHA1; LiHA2; LiHA3). The synthesis was conducted by the precipitation method according to the following reaction using reactants of analytical grade and double deionized water:



where $x = 0, 0.01, 0.04, 0.05$.

The diammonium hydrogen phosphate solution was added dropwise to the calcium and lithium nitrate solutions with continuous stirring using an overhead stirrer. The pH value of the reaction mixture was maintained at a level of 9.5–10.0 by adding aqueous ammonia. The powders were ripened in the mother solution for 21 days at a temperature of 37 °C for complete crystallization of the precipitate. The powders obtained were washed three times in deionized water, separated by vacuum suction filtration, and dried at 60 °C for 24 h and calcined at 900 °C for 1 h.

2.2. Powders characterizations

The chemical composition of the powders was investigated by inductively coupled plasma atomic emission spectroscopy (AES-ICP, HORIBA Jobin Yvon, ULTIMA 2) and ICP-OES Agilent 720. In addition, the flame photometry (PFA-378, Unico – Sis) was performed to confirm the lithium content according ICP. The powder materials were characterized by X-ray diffraction (XRD, Shimadzu 6000) with the identification of phase composition according to the ICDD PDF2 database. Peak indexing was carried out using the ICDD No 09–0432 card for HA. Fourier transform infrared absorption (FTIR) spectra of the samples were measured using the KBr technique on a Nicolet Avatar-330 FTIR spectrometer (Thermo Fisher Scientific) in the range from 4000 to 400 cm^{-1} to evaluate the functional groups of the powders. Conventional and pulsed X-band ($\nu_{\text{mw}} = 9.6 \text{ GHz}$) EPR measurements were performed out on a Bruker Elexsys E580 spectrometer.

2.3. DFT calculations

To calculate an equilibrated structure of HA, where Li^+ incorporation substitutes Ca^{2+} , the Density Functional Theory was used with the plane-wave basis and Vanderbilt ultrasoft pseudopotentials [16]. All calculations were performed using the Quantum ESPRESSO program [17]. The Perdew-Burke-Ernzerhof version of the generalized-gradient approximation of the exchange-correlation functional (GGA-PBE) [18] was used. The kinetic energy cutoffs of 45 Ry for the smooth part of the electron wave functions and of 300 Ry for the augmented electron density were set up (in agreement with previously mentioned [19]). The initial geometry for the HA and the unit cell parameters were taken from Ref. [20]. The results are illustrative for a $1 \times 1 \times 1$ monoclinic supercell, space group $\text{P}2_1/\text{m}$ with 88 atoms in the cell, which has previously been shown to be sufficient to reproduce spectra of doped HA crystals [21]. To estimate the effects of Li^+ incorporation on HA geometry, the geometries of HA supercell with Ca^{2+} substituted by Li^+ were calculated. To maintain the electroneutrality of the system, two possible schemes of charge compensation were considered. In one scheme the protonation of PO_4^{3-} group was changed, in the other a OH^- group was eliminated. The geometry optimization was performed with both the atomic positions and cell dimensions fully relaxed. The convergence condition on forces were 10^{-3} a.u. The Brillouin Zone integration was performed on a Monkhorst-Pack $2 \times 2 \times 1$ k-point mesh [22]. To determine the preferable positions of Li^+ incorporation, the energy difference was calculated by subtraction of the energy of system when Li^+ is in the Ca (2) from energy of system when Li^+ is in the Ca (1).

3. Results and discussion

3.1. Phase and chemical composition, functional groups descriptions

According to ICP-AES results, the chemical compositions of the synthesized powders were estimated as follows (Table 1). Except the lowest lithium content, the estimated values were closed to theoretical ones.

According to XRD (Fig. 1), the powders are characterized by a single HA phase (ICDD № 09–432). The introduction of Li⁺ had no noticeable effect on the degree of crystallinity of the materials. The calculation of the lattice parameters showed the negligible difference of the lattice parameters *a* and *c* in the Li⁺ doped materials compared to pure HA, characterized by the close values to the theoretical ones (Table 2). The similar absence of the strong effect regardless of the significantly smaller ionic radius of the Li⁺ cation compared to the Ca cation (Ca²⁺ - 0.104 nm) (Li⁺ - 0.068 nm) was previously observed for the low concentration of Li⁺ [14,23]. The calculation of D showed that the samples were formed by crystals with a size of 53–55 nm, regardless of the lithium content.

The FTIR spectra (Fig. 2) presented the typical vibrations previously demonstrated for HA and carbonated HA for all Li⁺ concentrations [14,24]. The materials were characterized by the presence of the well resolved stretching hydroxyl bands at 3571, 3493 and 633 cm⁻¹ indicating the complete formation of the hydroxyapatite structure. Surface P–OH bands were observed at 3648 and 3700 cm⁻¹ [25]. The ν_2 (H–O–H) was detected at 1635 cm⁻¹. The phosphate group is represented as stretching vibration modes ν_1 at 962 cm⁻¹, as a doublet of ν_3 region at 1089 cm⁻¹ and 1059 cm⁻¹, and latter shifted to 1061 cm⁻¹ upon Li⁺ content growth, as a band at 1044 cm⁻¹ and as a doublet at 565, and 601 cm⁻¹ of the O–P–O bending mode ν_4 , as well as the slightly poorly resolved triplet at 420–472 cm⁻¹ region of the double-generated bending mode ν_2 [26]. The additional stretching vibration band of the phosphate group at 1031 became visible, when lithium was introduced into the HA from 0.01 mol.%. The region between 1400 and 1575 cm⁻¹ bands and the narrow band at 875 cm⁻¹ for HA and LiHA1 correspond to carbonate groups with ν_2 [27], which could be adsorbed from air.

3.2. Electron paramagnetic resonance study

The EPR spectra of pure hydroxyapatite and with lithium ion impurities don't contain resonance absorption signals due to the absence of paramagnetic centers in the structure. Irradiation of the samples with an X-ray source leads to the formation of stable carbonate radicals with electron spins $S = \frac{1}{2}$ and an isotropic spectroscopic splitting factor $g = 2.009$ (1), whose pulse-mode EPR signal is shown in Fig. 3. The line shape and spectral width ($B_{FWHM} = 0.41$ mT) don't depend on the concentration of impurity lithium ions, indicating the absence of distortions in the crystal lattice. The dynamic (relaxation) properties T_1 (spin-lattice interaction) and T_2 (spin-spin interaction) of the carbonate centers don't change significantly for all three samples studied, further confirming the absence of modification of the lattice constants and the resulting side phases. The local nuclear environment of the carbonate radical was investigated by the electron spin echo envelope modulation (ESEEM) technique [14]. Fig. 3b shows the Fourier transform spectrum in the frequency domain containing signals from the structural nuclei of hydrogen ($^1H f = 14.7$ MHz, $I = 1/2$) and phosphorus ($^{31}P f = 6$ MHz) at a fixed magnetic field $B_0 = 341.4$ mT. The resonant signals arise from an anisotropic dipole-dipole interaction between the electron spin of the carbonate center and the nuclear spin. The obtained result confirms the presence of the investigated paramagnetic center in the crystal lattice, and not on the surface of the nanoparticles. A comparative analysis of the ESEEM spectra for two concentrations (0.1 and 1 mol.%) shows that the width of the nuclear resonance absorption lines remains the same, indicating a small change in the lattice constants. Fig. 3c shows the expanded spectrum in the stationary mode, where the resonance signal of the hydrogen radical H⁰ formed by the introduction of lithium ions was detected. The hydrogen radical has a characteristic isotropic hyperfine splitting of $A_{iso} = 50$ mT (1420 MHz) due to the Fermi contact interaction of the electron density with the nuclear magnetic moment. The formation of isolated hydrogen atoms is caused by one of the possible mechanisms of charge compensation, which consists in the release of anionic OH⁻ groups. The obtained experimental results correspond the DFT calculations presented below.

3.3. DFT calculations results

Foreigner cations may replace calcium ions in the Ca (1) or in the Ca (2) position of hydroxyapatite structure. There are six atoms of oxygen belonging to four orthophosphates in the Ca (1) position, which are coordinated with one calcium ion (Fig. 4a). It forms CaO6 prism geometry, a polyhedron intermediate between an octahedron and a trigonal prism. Considering the Ca (2) site, the calcium ion has seven oxygen atoms in the first coordination shell. Six of them are from four orthophosphate groups and one from a hydroxyl. The resulted CaO7 cluster expressed by distorted pentagonal bipyramid. The Ca²⁺–O distances are within 2.3–2.5 Å, in the Ca (2) position, calcium has a tighter environment.

If divalent calcium ions are substituted by monovalent lithium ion, an additional charge compensation is required. In the present

Table 1
The chemical composition of samples: theoretical and estimated by ICP-AES.

Sample	Theoretical formula	Estimated Li content, wt.%	Estimated formula
HA	Ca ₁₀ (PO ₄) ₆ (OH) ₂	0.000	Ca ₁₀ (PO ₄) ₆ (OH) ₂
LiHA1	Ca _{9.995} Li _{0.01} (PO ₄) ₆ (OH) ₂	0.005	Ca _{9.965} Li _{0.007} (PO ₄) ₆ (OH) ₂
LiHA2	Ca _{9.98} Li _{0.04} (PO ₄) ₆ (OH) ₂	0.027	Ca _{9.9805} Li _{0.039} (PO ₄) ₆ (OH) ₂
LiHA3	Ca _{9.975} Li _{0.05} (PO ₄) ₆ (OH) ₂	0.035	Ca _{9.975} Li _{0.050} (PO ₄) ₆ (OH) ₂

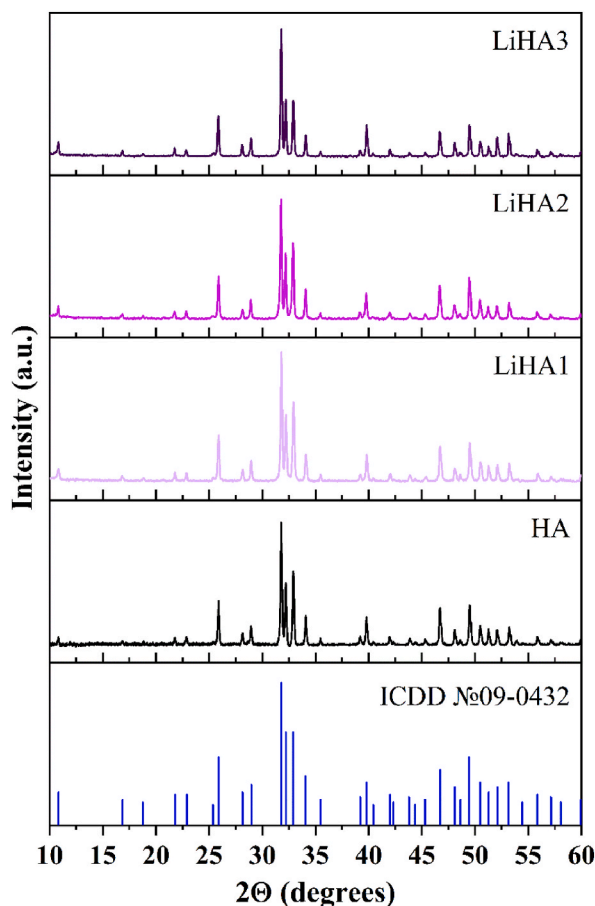


Fig. 1. The XRD diffractogram of the sample's powders after calcination at 900 °C for 1 h.

Table 2

The lattice parameters of samples.

Sample Code	a, nm	c, nm	c/a	V, nm ³
Standard HA (ICDD #09-0432)	0.9418	0.6884	0.7309	0.5287
HA	0.9421 (4)	0.6878 (3)	0.7300	0.5286
LiHA1	0.9421 (5)	0.6881 (3)	0.7303	0.5290
LiHA2	0.9426 (5)	0.6882 (5)	0.7299	0.5298
LiHA3	0.9424 (5)	0.6888 (5)	0.7309	0.5298

work we considered two schemes of charge compensation when Ca^{2+} is replaced by Li^+ to maintain the electroneutrality of the system: 1) an elimination of one OH^- group (Fig. 4b) 2) a protonation of one PO_4^{3-} group with resultant HPO_4^{2-} (Fig. 4c). In total, we had four principal molecular systems. In the former scheme Li^+ was in direct contact with one of oxygens but not with the hydrogen of HPO_4^{2-} .

Irrespective of the scheme of charge compensation used the inclusion of Li^+ in Ca (1) position is by ~ 0.2 eV more favorable than its inclusion into Ca (2) position.

The OH^- are located within the anion channel, surrounded by calcium ions, do not substantially influence the overall packing and the cell density. Insertion of Li^+ together with the release of OH^- caused a contraction of the cell size down to 1069.3 \AA^3 when Li^+ resides in Ca (1) position compared to the volume of 1073.7 \AA^3 in the pure HA cell. In contrast, when inserted in the Ca (2) position, Li^+ does not affect the cell dimensions (1073.8 \AA^3) compared to pure HA. Insertion of Li^+ together with HPO_4^{2-} causes a small expansion of the cell to 1076.4 \AA^3 in Ca (1) position and 1075.9 \AA^3 in Ca (2) position, probably due to extra hydrogen appearance. The density of the cell varies within $3.03\text{--}3.05 \text{ g/cm}^3$.

When cation inclusion occurs in Ca (1) position together with a phosphate replacement by HPO_4^{2-} , Li^+ position shifts to phosphate groups from original Ca^{2+} position by 0.703 \AA . In this position, Li^+ coordinates oxygen atoms of PO_4^{3-} groups at the following distances: $2.033, 2.062, 2.484, 2.581, 3.214, 3.266 \text{ \AA}$. Then the anion replacement is in the anion channel, which is remote from the

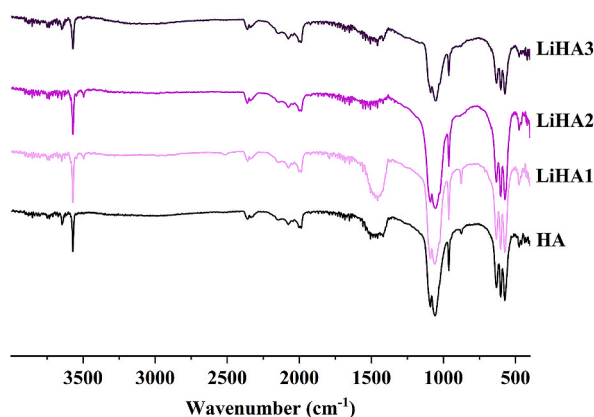


Fig. 2. FTIR spectra of the sample's powders after calcination at 900 °C for 1 h.

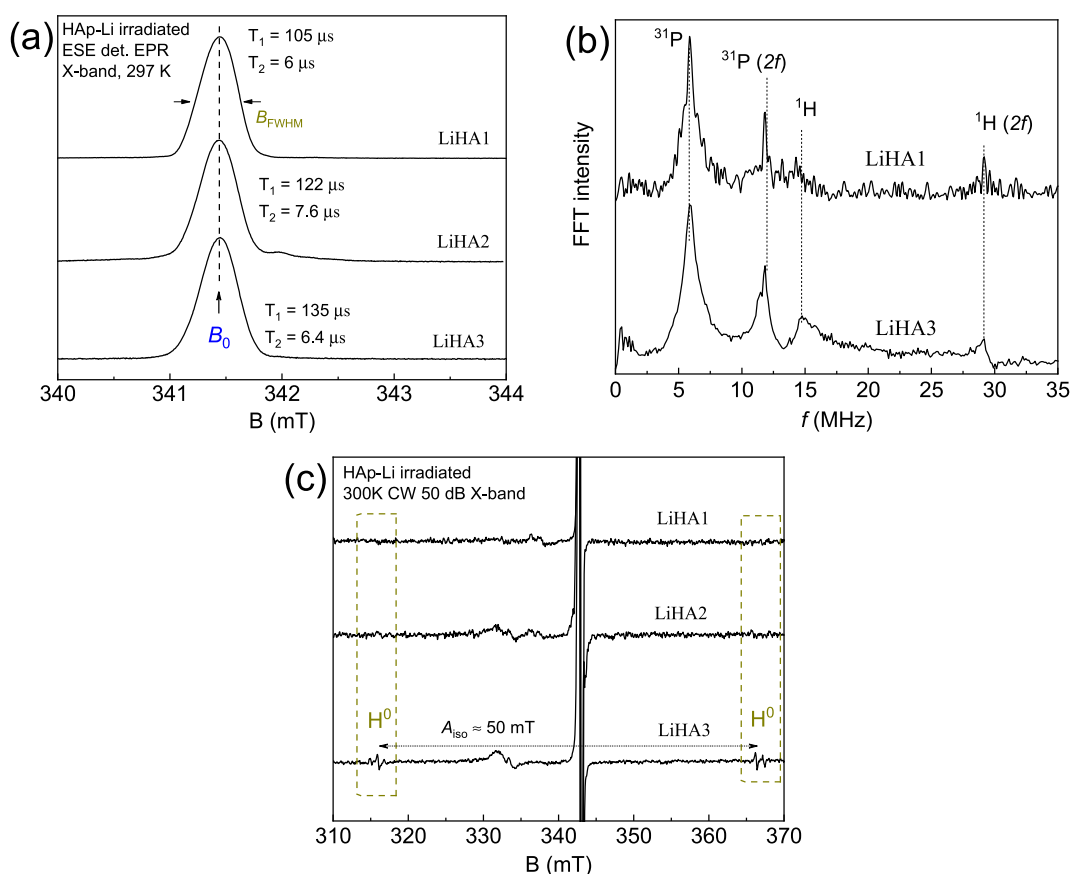


Fig. 3. (a) EPR spectra in the pulse mode of a radiation-induced center in LiHA samples. The inset shows the relaxation times for a fixed magnetic field $B_0 = 341.4$ mT; (b) ESEEM spectra in the frequency range with a magnetic field $B_0 = 341.4$ mT. The designation $2f$ indicates the presence of the second harmonic; (c) EPR spectra in stationary mode to demonstrate the presence of hydrogen radicals depending on Li ions concentration in HA.

lithium in Ca (1) position, Li^+ is shifted by 0.683 \AA towards phosphate groups, the coordination of oxygen atoms of PO_4^{3-} groups is as follows: 1.998, 2.051, 2.235, 2.897, 2.933, 3.244 \AA . To compare, the $\text{Ca}^{2+} \dots \text{O}$ shortest distances are within 2.3–2.5 \AA .

When lithium inclusion occurs in the Ca (2) position it also shifts towards the phosphate groups. The displacement is by 0.625 \AA when the phosphate is replaced by HPO_4^{2-} , and is by 0.646 \AA upon the elimination of OH^- group. The organization of oxygen atoms around the Ca (2) position is denser than around Ca (1) position. In line with that Li^+ in Ca (2) position coordinates oxygen atoms at shorter distances: 1.912, 1.922, 2.065, 2.726, and 3.148 \AA from the oxygen atoms of phosphate ions and 2.824 \AA from the oxygen atoms of OH^- , when charge compensation occurs with HPO_4^{2-} . When charge compensation is realized in the anion channel, Li^+

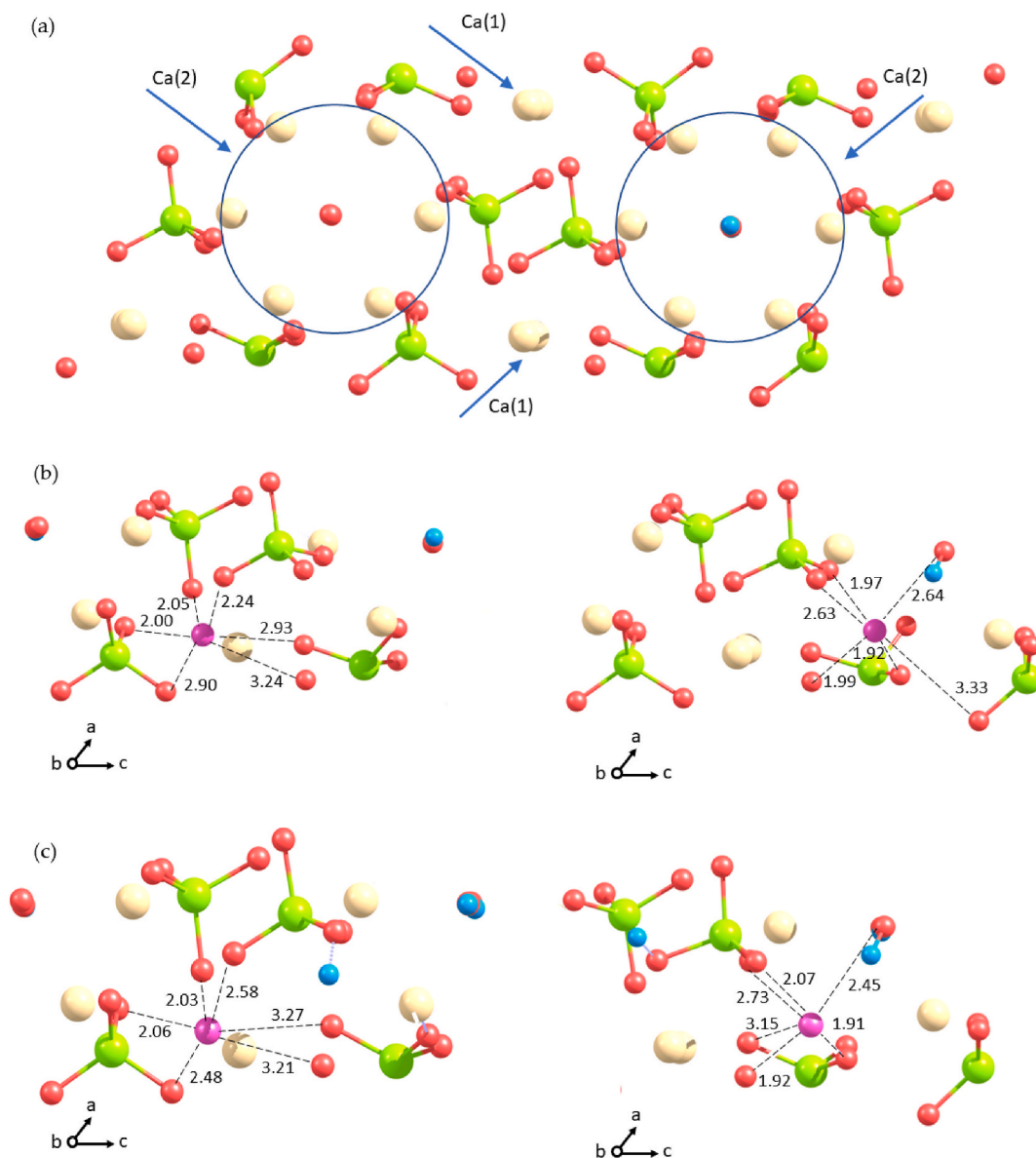


Fig. 4. (a) A periodic super-cell of HA, the calcium atoms in the circle are denoted as Ca (2), others as Ca (1). (b) substitution of Ca²⁺ by Li⁺ according to the scheme of charge compensation with OH⁻ release. The substitution in Ca (1) position (left) is by -0.28 eV more favorable than in Ca (2) position (right). (c) substitution of Ca²⁺ by Li⁺ according to the scheme of charge compensation with the HPO₄²⁻ formation. The substitution in Ca (1) position (left) is by -0.176 eV more favorable than in Ca (2) position (right). Color coding: yellow - Ca, green - P, red - O, cyan - H, magenta - Li. (For interpretation of the references to colour in this figure legend, the reader is referred to the Web version of this article.)

coordinates the oxygen atoms of phosphate groups at the following distances: 1.919, 1.965, 1.994, 2.630, and 3.334 Å, the distance to the oxygen of OH⁻ is 2.636 Å (which is longer than Ca...O, 2.39 Å). The distances of Li...O are shorter than Fe²⁺ ... O (1.98 Å) but longer than Fe³⁺ ... O (1.8 Å) [28].

In contrast to other cations that substitute for Ca²⁺ in HA, such as Fe [28], Al [19], Mg [29], the incorporation of Li⁺ significantly perturbs the anion channel. The insertion of Li⁺ into the Ca (2) position is coupled with the inclination of the closest OH⁻ group, which brings the H-atom closer to Li⁺ (at a distance of 2.45 Å in both schemes of charge compensation). The inclination can be characterized by the plane angle O...O-H, which decreases from 180° in pure HA to 133° in Li⁺ substituted HA. The shift of the H atom from its original position reaches 0.802 Å, while the O atom does not shifting from the axis of the anion channel. In the anionic channel, the distance of the pair O...O belonging to the hydroxyl groups closest to Li⁺ decreased from 3.35 Å to 2.92 Å. The O-H bond where the H atom is located between the oxygen atoms of the shortening O...O pair becomes as long as 0.992 Å (compared to 0.979 Å in unperturbed anion channel of pure HA), but the O-H linkage of the inclined to Li⁺ hydroxyl group becomes as short as 0.977 Å. These features of the geometry adjustment are strikingly different from those in the presence of other cations, where the oxygen atom of

hydroxyl shifts from the anion channel axis towards the cation to shorten the distance to the foreigner ion [19,28–30].

4. Conclusion

Attention to lithium-substituted HA has increased due to its high biomedical potential. At the same time, additional applications are growing, including materials for catalysis, adsorption, sensors and others are growing. The introduction of Li^+ into the calcium phosphate materials was associated with the need for charge balance compensation. In our work, we have synthesized Li^+ doped HA and demonstrated the preservation of the HA structure when up to 0.05 mol% Li^+ was introduced. The EPR study revealed the formation of isolated hydrogen atoms causing the release of anionic OH^- groups. The experimental results obtained were confirmed by DFT calculations. The two possible schemes of charge compensation when Ca^{2+} is replaced by Li to maintain the electroneutrality of the system were considered, based on the protonation of a PO_4^{3-} group and the elimination of an OH^- group. The results of the DFT calculations show an energy gain when Li^+ incorporates into the Ca (1) position, which accompanies with a small geometry perturbation. The energetically less probable positioning in the Ca (2) position leads to a drastic perturbation of the anion channel.

CRedit authorship contribution statement

Margarita A. Goldberg: Writing – original draft, Validation, Methodology, Conceptualization. **Marat R. Gafurov:** Writing – review & editing, Validation, Data curation. **Olga N. Makshakova:** Writing – original draft, Validation, Methodology, Formal analysis. **Sergey V. Smirnov:** Investigation. **Alexander S. Fomin:** Visualization, Investigation, Data curation. **Fadis F. Murzakhanov:** Writing – original draft, Methodology, Investigation. **Vladimir S. Komlev:** Writing – review & editing, Supervision, Conceptualization.

Declaration of competing interest

The authors declare that they have no known competing financial interests or personal relationships that could have appeared to influence the work reported in this paper.

Acknowledgments

The work was supported by the Russian Science Foundation, grant # 23-63-10056.

The authors are grateful to N. V. Ognevskaya for performing the ICP-AES investigations, and A. A. Fomina and N. A. Andreeva for flame photometry study.

References

- [1] M.U. Munir, S. Salman, A. Ihsan, T. Elsaman, Synthesis, characterization, functionalization and bio-applications of hydroxyapatite nanomaterials: an overview, *Int. J. Nanomed.* 17 (2022) 1903–1925, <https://doi.org/10.2147/IJN.S360670>.
- [2] E. Fiume, G. Magnaterra, A. Rahdar, E. Verné, F. Bairo, Hydroxyapatite for biomedical applications: a short overview, *Ceramics* 4 (2021) 542–563, <https://doi.org/10.3390/ceramics4040039>.
- [3] S. Mondal, U. Pal, 3D hydroxyapatite scaffold for bone regeneration and local drug delivery applications, *J. Drug Deliv. Sci. Technol.* 53 (2019) 101131, <https://doi.org/10.1016/j.jddst.2019.101131>.
- [4] M. Kay, R. Young, A. Posner, Crystal structure of hydroxyapatite, *Nature* 204 (1964) 1050–1052, <https://doi.org/10.1038/2041050a0>.
- [5] O. Kaygili, S. Keser, T. Ates, F. Yakuphanoglu, Synthesis and characterization of lithium calcium phosphate ceramics, *Ceram. Int.* 39 (2013) 7779–7785, <https://doi.org/10.1016/j.ceramint.2013.03.037>.
- [6] P. Clément-Lacroix, M. Ai, F. Morvan, S. Roman-Roman, B. Vayssi re, C. Belleville, K. Estrera, M.L. Warman, R. Baron, G. Rawadi, Lrp5-independent activation of Wnt signaling by lithium chloride increases bone formation and bone mass in mice, *Proc. Natl. Acad. Sci. U.S.A.* 102 (2005) 17406–17411, <https://doi.org/10.1073/pnas.0505259102>.
- [7] L. Li, X. Peng, Y. Qin, R. Wang, J. Tang, X. Cui, T. Wang, W. Liu, H. Pan, B. Li, Acceleration of bone regeneration by activating Wnt/ β -catenin signalling pathway via lithium released from lithium chloride/calcium phosphate cement in osteoporosis, *Sci. Rep.* 7 (2017) 1–12, <https://doi.org/10.1038/srep45204>.
- [8] V.P. Padmanabhan, T.S.N. Sankara Narayanan, S. Sagadevan, M.E. Hoque, R. Kulandaivelu, Advanced lithium substituted hydroxyapatite nanoparticles for antimicrobial and hemolytic studies, *New J. Chem.* 43 (2019) 18484–18494, <https://doi.org/10.1039/c9nj03735g>.
- [9] P. Keikhosravani, H. Maleki-Ghaleh, A.K. Khosrowshahi, M. Bodaghi, Z. Dargahi, M. Kavanlouei, P. Khademi-Azandehi, A. Fallah, Y. Beygi-Khosrowshahi, M. H. Siadati, Bioactivity and antibacterial behaviors of nanostructured lithium-doped hydroxyapatite for bone scaffold application, *Int. J. Mol. Sci.* 22 (2021), <https://doi.org/10.3390/ijms22179214>.
- [10] V.V. Smirnov, S.M. Barinov, S.V. Smirnov, A.I. Krylov, O.S. Antonova, M.A. Goldberg, T.O. Obolkina, A.A. Konovalov, A.V. Leonov, Structure and thermal stability of lithium-substituted hydroxyapatite ceramics, *Inorg. Mater.* 55 (2019) 715–723, <https://doi.org/10.1134/S0020168519070185>.
- [11] A.P.M. Shainberg, P. Val rio, A. Zonari, F.N. Oktar, L.S. Ozyegin, M.P.F. Gra a, M.F. Leite, A.M. Goes, Attachment and proliferation of osteoblasts on lithium-hydroxyapatite composites, *Adv. Mater. Sci. Eng.* (2012) 2012, <https://doi.org/10.1155/2012/650574>.
- [12] N. Matsumoto, K. Yoshida, K. Hashimoto, Y. Toda, Thermal stability of β -tricalcium phosphate doped with monovalent metal ions, *Mater. Res. Bull.* 44 (2009) 1889–1894, <https://doi.org/10.1016/j.materresbull.2009.05.012>.
- [13] V.V. Smirnov, S.V. Smirnov, A.I. Krylov, O.S. Antonova, M.A. Goldberg, T.O. Obolkina, A.A. Konovalov, A.V. Leonov, S.M. Barinov, Influence of lithium on the structure and phase composition formation in the synthesis of hydroxyapatite, *Dokl. Chem.* 481 (2018) 177–180, <https://doi.org/10.1134/S0012500818080025>.
- [14] N. Salam, I.R. Gibson, Lithium ion doped carbonated hydroxyapatite compositions: synthesis, physicochemical characterisation and effect on osteogenic response in vitro, *Biomater. Adv.* 140 (2022) 213068, <https://doi.org/10.1016/j.bioadv.2022.213068>.
- [15] M.A. Goldberg, O.S. Antonova, N.O. Donskaya, A.S. Fomin, F.F. Murzakhanov, M.R. Gafurov, A.A. Konovalov, A.A. Kotyakov, A.V. Leonov, S.V. Smirnov, T. O. Obolkina, E.A. Kudryavtsev, S.M. Barinov, V.S. Komlev, Effects of various ripening media on the mesoporous structure and morphology of hydroxyapatite powders, *Nanomaterials* 13 (2023), <https://doi.org/10.3390/nano13030418>.
- [16] D. Vanderbilt, Soft self-consistent pseudopotentials in a generalized eigenvalue formalism, *Physical Review B, Rapid Communications* 41 (1990) 7892–7895, [https://doi.org/10.1016/S0016-5085\(77\)80340-5](https://doi.org/10.1016/S0016-5085(77)80340-5).

- [17] P. Giannozzi, S. Baroni, N. Bonini, M. Calandra, R. Car, C. Cavazzoni, D. Ceresoli, G.L. Chiarotti, M. Cococcioni, I. Dabo, A. Dal Corso, S. De Gironcoli, S. Fabris, G. Fratesi, R. Gebauer, U. Gerstmann, C. Gougoussis, A. Kokalj, M. Lazzeri, L. Martin-Samos, N. Marzari, F. Mauri, R. Mazzarello, S. Paolini, A. Pasquarello, L. Paulatto, C. Sbraccia, S. Scandolo, G. Sclauzero, A.P. Seitsonen, A. Smogunov, P. Umari, R.M. Wentzcovitch, Quantum ESPRESSO: a modular and open-source software project for quantum simulations of materials, *J. Phys. Condens. Matter* 21 (2009), <https://doi.org/10.1088/0953-8984/21/39/395502>.
- [18] J.P. Perdew, K. Burke, M. Ernzerhof, Generalized gradient approximation made simple, *Phys. Rev. Lett.* 77 (1996) 3865–3868, <https://doi.org/10.1103/PhysRevLett.77.3865>.
- [19] M. Goldberg, M. Gafurov, O. Makshakova, V. Smirnov, V. Komlev, S. Barinov, E. Kudryavtsev, N. Sergeeva, S. Achmedova, G. Mamin, F. Murzakhanov, S. Orlinskii, Influence of Al on the structure and in vitro behavior of hydroxyapatite nanopowders, *J. Phys. Chem. B* 123 (2019) 9143–9154, <https://doi.org/10.1021/acs.jpcc.9b08157>.
- [20] M. Yashima, Y. Yonehara, H. Fujimori, Experimental visualization of chemical bonding and Structural.pdf, *J. Phys. Chem. C* 115 (2011) 25077–25087.
- [21] T. Biktagirov, M. Gafurov, G. Mamin, E. Klimashina, V. Putlayev, S. Orlinskii, Combination of EPR measurements and DFT calculations to study nitrate impurities in the carbonated nanohydroxyapatite, *J. Phys. Chem. A* 118 (2014) 1519–1526, <https://doi.org/10.1021/jp410900m>.
- [22] H.J. Monkhorst, J.D. Pack, Special points for Brillouin-zone integrations, *Phys. Rev. B* 13 (1976) 5188–5192, <https://doi.org/10.1103/PhysRevB.16.1748>.
- [23] H. Badran, I.S. Yahia, M.S. Hamdy, N.S. Awwad, Lithium-doped hydroxyapatite nano-composites: synthesis, characterization, gamma attenuation coefficient and dielectric properties, *Radiat. Phys. Chem.* 130 (2017) 85–91, <https://doi.org/10.1016/j.radphyschem.2016.08.001>.
- [24] A. Sroka-Bartnicka, L. Borkowski, G. Ginalska, A. Ślósarczyk, S.G. Kazarian, Structural transformation of synthetic hydroxyapatite under simulated in vivo conditions studied with ATR-FTIR spectroscopic imaging, *Spectrochimica Acta - Part A: Molecular and Biomolecular Spectroscopy* 171 (2017) 155–161, <https://doi.org/10.1016/j.saa.2016.07.051>.
- [25] M.A. Goldberg, P.V. Protsenko, V.V. Smirnov, O.S. Antonova, S.V. Smirnov, A.A. Kononov, K.G. Vorckachev, E.A. Kudryavtsev, S.M. Barinov, V.S. Komlev, The enhancement of hydroxyapatite thermal stability by Al doping, *J. Mater. Res. Technol.* 9 (2020) 76–88, <https://doi.org/10.1016/j.jmrt.2019.10.032>.
- [26] J.V. Rau, V.M. Wu, V. Graziani, I.V. Fadeeva, A.S. Fomin, M. Fosca, V. Uskoković, The Bone Building Blues: self-hardening copper-doped calcium phosphate cement and its in vitro assessment against mammalian cells and bacteria, *Mater. Sci. Eng. C* 79 (2017), <https://doi.org/10.1016/j.msec.2017.05.052>.
- [27] S. Kongsri, K. Janpradit, K. Buapa, S. Techawongstien, S. Chanthai, Nanocrystalline hydroxyapatite from fish scale waste: preparation, characterization and application for selenium adsorption in aqueous solution, *Chem. Eng. J.* 215–216 (2013) 522–532, <https://doi.org/10.1016/j.cej.2012.11.054>.
- [28] M.A. Goldberg, A.V. Akopyan, M.R. Gafurov, O.N. Makshakova, N.O. Donskaya, A.S. Fomin, P.P. Polikarpova, A.V. Anisimov, F.F. Murzakhanov, A.V. Leonov, A.A. Kononov, E.A. Kudryavtsev, S.M. Barinov, V.S. Komlev, Iron-doped mesoporous powders of hydroxyapatite as molybdenum-impregnated catalysts for deep oxidative desulfurization of model fuel: synthesis and experimental and theoretical studies, *J. Phys. Chem. C* 125 (2021) 11604–11619, <https://doi.org/10.1021/acs.jpcc.1c01338>.
- [29] M.A. Goldberg, A.S. Fomin, F.F. Murzakhanov, O.N. Makshakova, N.O. Donskaya, O.S. Antonova, O.I. Gnezdilov, I.V. Mikheev, A.V. Knotko, E.A. Kudryavtsev, S.A. Akhmedova, I.K. Sviridova, N.S. Sergeeva, G.V. Mamin, S.M. Barinov, M.R. Gafurov, V.S. Komlev, The improved textural properties, thermal stability, and cytocompatibility of mesoporous hydroxyapatite by Mg²⁺ doping, *Mater. Chem.* 289 (2022) 126461, <https://doi.org/10.1016/j.matchemphys.2022.126461>.
- [30] O.N. Makshakova, M.R. Gafurov, M.A. Goldberg, The mutual incorporation of Mg²⁺ and CO₃²⁻ into hydroxyapatite: a DFT study, *Materials* 15 (2022), <https://doi.org/10.3390/ma15249046>.